Published in final edited form as:
Heart Rhythm. 2014 January ; 11(1): 150–157. doi:10.1016/j.hrthm.2013.09.071.

In-vitro Photoacoustic Visualization of Myocardial Ablation Lesions

Nicholas Dana, BSc[1,2], **Luigi Di Biase, MD, PhD, FHRS**[1,3,4,5], **Andrea Natale, MD, FHRS**[1,3], **Stanislav Emelianov, PhD**[1,2], and **Richard Bouchard, PhD**[1,2]

[1]Department of Biomedical Engineering, University of Texas at Austin, Austin, TX, USA

[2]Department of Imaging Physics, University of Texas MD Anderson Cancer Center, Houston, TX, USA

[3]Texas Arrhythmia Institute, St. David's Medical Center, Austin, TX, USA

[4]Department of Cardiology, University of Foggia, Foggia, Italy

[5]Albert Einstein College of Medicine, Montefiore Hospital, New York City, New York, USA

Abstract

Background—Radiofrequency (RF) ablation to treat atrial arrhythmia is limited by an inability to reliably assess lesion durability and transmurality.

Objective—Determine feasibility of photoacoustic characterization of myocardial ablation lesions *in vitro*. In this study, we investigate the feasibility of combined ultrasound (US) and spectroscopic photoacoustic (sPA) imaging to visualize RF ablation lesions in 3-D based on unique differences in the optical absorption spectra between normal and ablated myocardial tissue.

Methods—Tissue samples were excised from the ventricles of fresh porcine hearts. Lesions were generated using an RF catheter ablation system using 20 - 30 W of power applied for 40 - 60 s. Ablated samples were imaged in the NIR regime (740-780 nm) using a combined PA/US imaging system. Measured PA spectra were correlated to the absorption spectra of deoxy-hemoglobin and ablated tissue to produce a tissue characterization map (TCM) identifying 3-D lesion location and extent. Tissue samples were stained and photographed for gross pathology. TCM and gross pathology images were co-registered to assess TCM accuracy.

Corresponding Author: Dr. Richard Bouchard Department of Imaging Physics University of Texas MD Anderson Cancer Center 1881 East Rd. Unit 1902 Houston, TX 77054 Phone: (713) 745-0626 Fax: (713) 563-2986 RRBouchard@mdanderson.org.

Author disclosure and conflict of interest:
N. Dana: None; **R. Bouchard**: None; **S. Emelianov**: None; **L. Di Biase**: A - Consulting Fees/Honoraria; 2; Biosense Webster, Inc., Hansen Medical; **A. Natale**: A - Consulting Fees/Honoraria; 1; Medtronic, Inc., Biotronik, St. Jude Medical. A -Consulting Fees/ Honoraria; 2; Biosense Webster, Inc., Boston Scientific Corp.

Results—The TCM reliably characterized ablated and non-ablated tissue up to depths of 3 mm. The TCM also assessed lesion position and extent with sub-millimeter accuracy in multiple dimensions. Segmented TCMs achieved greater than 69% agreement with gross pathology.

Conclusion—These results suggest that sPA imaging has the potential to accurately assess RF ablation lesion size and position with sub-millimeter precision and may be well suited to guide trans-catheter RF atrial ablation in clinical practice.

Keywords

Ablation; Atrial fibrillation; Radiofrequency; Imaging; Photoacoustic; Tissue characterization

Introduction

Atrial Fibrillation

Atrial fibrillation (AF) is currently the most common arrhythmia encountered in clinical practice, with estimates as high as 6.1 million sufferers in 2010 in the United States alone (1,2). AF has been implicated in an increased risk of stroke, dementia, heart failure and an excess mortality rate (1,3–5). Anti-arrhythmic drugs are burdened with significant side effects, toxicity and poor capability to maintain NSR and thus are not the ideal treatment option for AF patients (6–8). Radio-frequency (RF) trans-catheter ablation is currently the most effective treatment for AF (6) as it can isolate the firing of ectopic foci, typically located around the pulmonary veins (9,10). Unfortunately, RF ablation lesions can vary considerably with catheter contact force, orientation, size and RF energy parameters (6,11,12). Lesion “reconnection” and “recovery” has been a major cause for procedural failure and can necessitate repeat procedures (6,7). Furthermore, ablation procedures carry the risk of severe complications, such as atrio-esophageal fistulae or cardiac tamponade (6,7). These limitations of RF trans-catheter ablation will not be significantly improved without a real-time (RT) tool to characterize lesions intraoperatively (6).

Several attempts have recently been made to address this need by probing changes that occur in tissue as RF energy denatures proteins and disrupts native structure. MRI has been used both to guide RF trans-catheter ablation (13) and to provide thermographic information (14).

Unfortunately, MRI for these applications tends to suffer from poor spatial resolution and low frame rates (1.8 mm and < 5 frames per second [fps], respectively, for real-time MRI and 1.7 mm and < 1 frame per 4 cardiac cycles, respectively, for MRI thermography) (13,14). Additionally, both techniques require the advent of MRI compatible equipment (13,14), and long-duration MRI studies can be cost prohibitive.

Optical coherence tomography (OCT) is being investigated as a means to assess lesion formation and provide real-time feedback to physicians during ablation procedures (15). OCT relies on back-scattered light from a coherent source to interrogate tissue optical properties. The reliance on quasi-ballistic photon propagation limits OCT by imposing a maximum imaging depth of approximately 1 mm (15), restricting the use of OCT to only atrial regions where tissue is thinnest and limiting assessment of transmurality. Acoustic

radiation force impulse (ARFI) imaging is an ultrasound (US)-based elasticity imaging technology being investigated as a means to intraoperatively identify RF ablation lesions (16,17). ARFI imaging interrogates mechanical properties by analyzing the ARFI-induced dynamic response of tissue. ARFI relies on micrometer-order tissue displacement, making it particularly susceptible to motion artifacts, that results in a significant fraction of unusable images (17).

Photoacoustic Imaging

Photoacoustic (PA) imaging is making inroads as a novel medical imaging technique utilizing short-duration laser pulses (18,19) which are absorbed by chromophores (such as deoxy-hemoglobin [Hb]) in the tissue, resulting in thermoelastic expansion and generation of an acoustic transient (18,19). These local transients can be imaged using a traditional US transducer (20–22), providing an optical absorption map with resolutions on the order of tens of micrometers (or hundreds of micrometers using a 7.5 MHz US probe, which is common for EP intracardiac or transesophageal US applications and comparable to MRI) and at imaging depths in excess of a centimeter (18–22).

The peak photoacoustic pressure, generated during thermal and stress confinement, is commonly modeled as

$$p_0(\mathbf{r},\lambda) = \left(\frac{\beta(T)\, v_s^2(T)}{C_p(T)}\right) \mu_{abs}(\mathbf{r},\lambda)\, \Phi(\mathbf{r},\lambda) \quad \text{Eq. 1}$$

where $\beta(T)$ [K^{-1}] is the temperature dependent thermal coefficient of volume expansion, $v_s(T)$ [cm s^{-1}] is the sound velocity in tissue, $C_p(T)$ [J kg^{-1} K^{-1}] is the heat capacity at constant pressure, μ_{abs} ($\mathbf{r}$, λ) [cm^{-1}] is the optical absorption coefficient and Φ ($\mathbf{r}$, λ) [J cm^{-2}] is the local optical fluence (18,19). As such, $\mathbf{r}$, λ and T represent spatial distribution, optical wavelength and temperature, respectively.

PA imaging contrast is provided by variations in optical absorption (μ_{abs}) resulting from variations in the concentration of endogenous or exogenous chromophores. Due to the wavelength dependence of μ_{abs}, spectroscopic photoacoustic imaging (sPA) can be performed for tissue characterization purposes (23–25). PA imaging's reliance upon ultrasonic sensing allows straightforward co-registration with anatomical US images, providing molecularly sensitive anatomical PA/US images (20–22). For these reasons, PA imaging is being pursued as a powerful medical imaging modality in cancer detection (26), disease staging (22) and therapy monitoring (21).

Methods

Sample preparation and ablation

Fresh porcine hearts (Sierra for Medical Science, Whittier, CA) were acquired within 24 hours of sacrifice and were never frozen. The ventricles were harvested and samples were excised from these portions to produce approximately 20×20×10 mm^3 sized specimens for ablation. The ablation system consisted of a Stockert 70 RF generator combined with a COOLFLOW® irrigation pump and a THERMOCOOL® irrigated tip catheter (Biosense

Webster Inc., Diamond Bar, CA). During each ablation, the catheter was flushed with PBS. RF energy was applied at a rate of 20 - 30 W for 40 - 60 s. Tissue samples were submerged in normal PBS during ablation and then patted dry and returned to an airtight container and refrigerated.

Imaging system setup and procedure

Normal PBS was used to acoustically couple the imaging system with the tissue. Imaging was performed on a combined PA/US imaging system that consisted of a Vevo® 2100 US imaging system (FUJIFILM VisualSonics Inc., Toronto, ON, Canada) paired with an LZ-250 transducer (21-MHz center frequency) with integrated fiber optics connected to a pulsed, tunable Nd:YAG laser (680 - 970 nm wavelength range). A single three-dimensional (3-D) combined PA/US B-mode scan was performed on each sample at 710 nm. From that 3-D volume, a single 2-D plane corresponding to the brightest region of the PA signal was selected for sPA imaging from 680 - 840 in 2-nm steps. Ten frames were averaged into a single PA/US image at each sampled wavelength (Figures 1B, 2A and 3B). Energy was measured at the fiber bundle output using an external power meter. This protocol was used to image eight ablated samples harvested from two porcine hearts. Later, a full 3-D PA/US volume was acquired for each wavelength from 740 – 780 nm in 5-nm steps. At each wavelength, six PA/US volumes were averaged. The resulting 3-D sPA data were normalized to the average laser energy at each corresponding wavelength. This second protocol was used to image six ablated samples from two additional porcine hearts. A schematic of the imaging system is shown in Figure 1.

Sample staining procedure

For the purpose of sample staining, nitro-tetrazolium blue (NTB) salt (Sigma-Aldrich Corp., St. Louis, MO) was chosen to identify macroscopic myocardial tissue necrosis (27). The NTB solution was prepared by dissolving NTB in normal PBS at 0.5 mg ml^{-1} and maintained at 35 C°, as outlined by Ramkissoon (27). All specimens were incubated in the NTB solution for 15 minutes, then patted dry and photographed for gross pathology.

ROI selection and analysis

Equal-sized regions-of-interest (ROIs; 0.04 mm^2) of the PA signal center (Ablated) and a specimen region external to the lesion (Non-ablated) were selected from the 2-D sPA dataset for analysis, as shown in the white boxes in Figure 2A.

Contrast and reference spectra

Contrast-to-background ratio (CBR) was calculated using the mean PA signal intensity for the Ablated and Non-ablated ROIs. To obtain PA signal spectra, the mean PA intensities for both ROIs were calculated and plotted as a function of wavelength; Figure 2B shows representative spectra observed in Ablated (red) and Non-ablated (blue) myocardium (normalized for display purposes). These spectra differ considerably near 760 nm, where the Non-ablated spectrum has a prominent hump, which correlates well with the extinction spectrum of Hb (28), and is absent from the Ablated spectrum. For this reason, two spectra (Figure 2D) were selected for a Pearson correlation test to characterize the two tissue types.

Ablated reference spectra were obtained by averaging ROIs from ablated samples ($n = 8$) harvested from two separate hearts. The known extinction spectrum for Hb was normalized and used as a reference for the non-ablated tissue.

sPA image processing and correlation

Prior to the correlation test, each sPA dataset was filtered spatially and to reduce noise. For the 3-D sPA data, each 3-D volume was filtered using a 3-D sliding average kernel. Voxel-by-voxel correlation, using both the Ablation-reference and the Hb-reference spectra, was performed on each 2-D and 3-D sPA dataset through 740 - 780 nm. For each sPA dataset, Ablation reference and Hb reference correlation maps were obtained. A final tissue characterization map (TCM, Figure 2C) was then generated. Voxels of the TCM showing high ($r \geq 0.65$) Ablation-reference or Hb-reference correlation were displayed as either red or blue, respectively, whereas voxels showing high correlation to both spectra were color coded green. TCM voxels showing poor correlation ($r < 0.65$) to both spectra were not color coded. For each voxel that correlated to either Ablation or Hb reference spectra, the *p*-value of the correlation was calculated based on the null hypothesis. 3-D rendering of the data (Figure 4A and 4B) was achieved with Amira (VSG, Burlington, MA); a clipping plane was introduced at the location of the tissue bisection (Figure 4B) to compare 3-D TCMs with the side-view gross pathology (Figure 4D).

Image registration and comparison

Three-dimensional TCM/US data was co-registered with matching photographed gross pathology. Gross pathology photographs were acquired in top-view and side-view orientations. Both orientations were adjusted so that the gross pathology field of view (FOV) represented the same FOV as the US volume. In the top-view gross pathology images, tissue sample boundaries and the ablated region were manually segmented from the photograph background (Figure 3A, blue and red, respectively) and a line was placed to identify the tissue bisection plane. An equivalent top-view orientation was then reconstructed using the TCM/US volume data with matching segmentations performed on this reconstructed view.

A straightforward rigid image registration was applied to both top- and side-view image sets. Once the top-view gross pathology and matched TCM/US data were co-registered, an image slice was selected from the TCM/US data that corresponded to the tissue bisection plane. A similar segmentation and registration process was then performed on the side-view gross pathology and selected TCM/US data (Figures 3C and 3D, respectively).

Once both the top- and side-view image sets were co-registered, the accuracy of the TCM was determined. The centroids of the ablated-region segmentations were calculated for each gross pathology and TCM set. For each co-registered set, the lateral, axial and elevation offsets between the centroids were measured. Agreement between the segmentations was assessed by comparing the maximum axial, lateral or elevation extent of the segmented region. The % Area Agreement was defined as the area of the segmentations' intersection divided by the area of the segmentations' union. For the side-view co-registered samples, two samples were utilized to assess elevation offset, while four samples were utilized to

assess lateral offset; all six side-view co-registered samples were utilized to assess axial offset.

Results

Single-wavelength analysis

Figure 2A shows a representative single-wavelength combined PA/US image acquired at 710 nm. Based on matched gross pathology images of the stained sample, the red-orange region located at the image center, at approximately 11 mm depth, correlates to the core of the lesion.

For Figure 2A, $\overset{\mathrm{G}}{I}_{Abl} = -7.8 \pm 3.0 \quad dB$, $\overset{\mathrm{G}}{I}_{Nabl} = -38.6 \pm 2.4 \quad dB$ (both normalized to the PA signal peak intensity at 710 nm), and CBR is 30.7 ± 3.1 dB.

Spectroscopic analysis

Both normalized spectra from the ROIs in Figure 2A are shown in Figure 2B. The Ablated absorption spectrum monotonically decreases, which agrees with results obtained by Swartling, et al. (24) The Non-ablated absorption spectrum agreed well with that of Hb (28), notably displaying a prominent hump near 760 nm. In this wavelength range, Hb is expected to be the dominant absorber in a harvested (i.e. oxygen depleted) myocardial sample.

An example of the TCM overlaying the corresponding B-mode US image is displayed in Figure 2C. The correlation maps demonstrate the ability to visualize both ablated and non-ablated tissue at greater depth and extent than that afforded by single-wavelength PA images. Figure 2C indicates, at lateral positions of 6 mm and 10.5 mm, the correlation protocol was able to identify 2 - 3 mm of ablated myocardium beneath at least an additional millimeter of non-ablated myocardium. This was typical of both 2-D and 3-D imaged samples, where the sPA data showed good correlation to absorbers up to a depth of 3 mm. The average correlation *p*-value over all voxels was 0.0104 ± 0.0098, suggesting that the overall correlation was highly significant.

Lesion dimension statistics

The results of the 3-D segmentation comparison are shown in Table 1. For the top-view orientation (Figures 3A and 3B), good agreement between the gross pathology images and TCM was achieved, with no elevation and low lateral (0.4 mm) offset measured. The absolute difference between the average lateral and elevation extent was 1 mm or less, and well within the standard deviations for both measurements. The mean segmented lesion areas were calculated to be 37.8 ± 15.8 mm^2 and 41.8 ± 16.4 mm^2 for the TCM and gross pathology, respectively. The difference between these areas was 4.0 mm^2 (approximately 10% total lesion area), which is within the standard deviations of both measurements. The % Area Agreement, as defined in Equation 3, was approximately 70% averaged across all 6 samples, indicating good TCM and gross pathology agreement for all 3-D volumes.

For the side-view orientation (Figures 3C and 3D), the two samples cut parallel to the elevation axis showed an average of a 0.9-mm offset in that dimension. The samples cut

laterally showed good lateral agreement (offset of 0.1 mm). The axial dimension showed the greatest offset, averaging 1.2 mm across all 6 samples. The average axial extent of the lesion segmentations was 3.4 ± 1.0 mm and 5.3 ± 1.0 mm, for the TCM and gross pathology, respectively. Mean segmented areas were calculated to be 14.5 ± 4.9 mm^2 and 30.7 ± 10.1 mm^2 for the TCM and gross pathology, respectively, while the % Area Agreement was 36% (averaged across 6 samples).

The 3-D rendered data compared well with the matching gross pathology (Figures 4A-D). In this data set, there are two distinct regions of ablated tissue surrounded by non-ablated tissue and separated by an approximately 2-mm non-ablated gap (Figure 4A). The tissue is also consistently identified to depths greater than 2 mm, for both ablated and non-ablated myocardium, and generally agrees well with the matched gross pathology (Figure 4C and 4D).

Discussion

Single-wavelength PA imaging shows high contrast from the lesion core, which indicates it may be useful as a pilot scan to locate the approximate lesion center, but it lacks the ability to fully differentiate ablated vs. non-ablated myocardium. In comparison, the sPA-based TCM demonstrated the ability to reliably identify ablated and non-ablated myocardium with high accuracy and sub-millimeter precision (Figures 2C, 3B, 3D, 4A and 4B). TCM images of ablated and non-ablated tissue appear relatively uniform across the entire imaged area or volume (Figures 2C, 3B, 3D, 4A and 4B). All TCM images showed consistent tissue characterization and correlated well to matched images of gross pathology to at least 2 mm in depth (Figures 2C, 3 and 4).

One caveat of PA imaging is that imaging artifacts, resulting from refractive index discontinuities, can occasionally be seen near tissue boundary locations. These artifacts, however, would be minimal in an *in vivo* environment, as the imaging target would not be an explanted tissue sample with tissue-solution boundaries. Also, spectroscopic-based images, such as a TCM, may further reduce artifacts by correlating multiple wavelengths and reducing the effects of saturated voxel regions by identifying absorbers. It should also be noted that the particular imaging system used has reduced SNR at the left and right frame edges, which also contributes to image artifacts in the TCM as broadband noise weakly correlates with the Ablated spectrum. Given the 3-D datasets (Figures 3B, 3D, 4A and 4B) were acquired using only six averages and without laser energy pulse-to-pulse normalization, increased frame averaging, improved energy normalization and increased surface fluence should improve TCM quality and increase depth penetration beyond 3 mm. Given its depth penetration capabilities, PA imaging may be best suited for guidance of trans-catheter ablation of atrial arrhythmia.

When considering the segmentation metrics, it should be first noted that a basic rigid registration method was utilized that did not account for tissue deformation, which will inherently introduce error. Despite this limitation, excellent agreement was achieved with the top-view comparisons, with no elevation and small lateral offset observed. Furthermore, the average top-view segmented areas differed only by 4 mm^2, yielding a % Area

Agreement of 69 ± 11%; this area agreement is comparable with other lesion imaging methods currently being developed (16). For the side-view orientation, lateral offset was improved when compared to the top-view orientation (0.1 mm vs. to 0.4 mm). The relatively high axial offset (1.2 mm) observed in this orientation is attributable to the limited ability in this initial implementation of sPA imaging to characterize tissue at depths greater than 3 mm; this penetration depth can be increased with improved frame averaging, improved energy normalization and increased laser fluence. With said improvements the ability of this imaging modality to reliably characterize tissue and assess transmurality at depths > 3 mm could be determined. As can be seen in Figure 3C and 4D, the ablated regions extend axially from approximately 10 mm to 15 mm and 11 mm to 16 mm, respectively (5 mm in both instances). The deepest 2 mm of ablated myocardium was not visualized, so the axial position of the segmented TCM centroid naturally appears shallow compared to the centroid of the segmented lesion from photographed gross pathology. This also accounts for the lower % Area Agreement score (36%) when compared with the top-view results (69%).

The 3-D rendering (Figures 4A and 4B) of the dual-lesion data gave the opportunity to examine the ability of the system to identify adjacent lesions. We can clearly see two distinct regions, approximately 4 mm in diameter each, which correlate strongly to the Ablated reference (red); surrounding these two regions is tissue that consistently correlates to the Non-ablated reference (blue). This segmentation agrees well with gross pathology images, shown in Figures 4C and 4D. Additionally, a small region of tissue that correlates to both reference spectra is seen lying between the two lesions in Figure 4B (green). This segmentation agrees well with matching gross pathology (Figure 4D), as a small isthmus of ambiguous tissue lies between the two lesions (approximately 11 mm in the axial and elevation dimensions). This result emphasizes the ability of sPA to identify regions where lesion contiguity may be in question.

Given that the PA spectrum observed in ablated tissue results from bulk hyperthermia-induced protein denaturation, resulting from tissue heating, it is believed that this spectrum would not vary significantly from patient to patient, nor vary significantly between normal or pathologic myocardium. Also, given that thermal damage generally eliminates the observed birefringence resulting from myocardial muscle-fiber orientation, it is believed that PA imaging would be insensitive to fiber orientation.

Study limitations and future work

There are several still unexamined aspects of using PA imaging to guide trans-catheter ablation of atrial arrhythmia. Clearly any tool used to guide trans-catheter ablation must be RT or near-RT, and in this initial work we have not examined using PA imaging during RF lesion creation. PA imaging frame rate is practically limited by the pulse repetition frequency of the irradiating laser source (10-20 Hz in this initial setup). Our initial system is capable of providing near-RT imaging (1-2 fps each consisting of 11 optical wavelengths with no averaging), and many laser systems, operating at kHz frequencies, are currently available that could provide RT PA imaging. Once studies have demonstrated which wavelengths are optimal for *in vivo* imaging, a system could be constructed using several diode lasers, operating at kHz pulse repetition rates, to provide frame rates well in excess of

30 fps. Still unexamined is the feasibility of using PA imaging to characterize cryoablation lesions. Since little research has been done to directly compare the optical absorption of hyper- versus hypothermia-induced myocardial lesions, further studies must be conducted to assess the feasibility of using this method to characterize cryoablation myocardial lesions. Another consideration is the translation of PA imaging to an *in vivo* environment, which will present practical hurdles. In an *in vivo* environment, the ablation and imaging substrate will be highly oxygenated tissue. Given that the optical absorption of oxy-Hb can be nearly an order of magnitude less in the NIR regime (26), when compared to deoxy-Hb, one could expect that the background signal may be lower in highly oxygenated tissue.

While this may require modification of the wavelengths chosen to image, if the spectrum of ablated tissue remains unchanged *in vivo*, then an *in vivo* environment could provide greater PA signal contrast between ablated and non-ablated tissue. *In vivo* applications of PA imaging have already demonstrated feasibility of PA imaging through luminal blood using relatively low optical fluences and observing minimal signal from blood (22). An ICE implementation of PA imaging could achieve higher fluences than previous studies (22), and optical scattering due to blood may aid in homogenizing optical fluence at the endocardial surface. As with other clinical imaging modalities (US, MRI, CT), PA imaging can be implemented using a cardiac gating function to minimize motion between frames as well to reduce optical changes resulting from the cardiac perfusion cycle. Although the technical integration of an intracardiac probe capable of concurrent ablation and PA imaging will not be trivial, the development of such a clinical probe should be possible given recent advances in combined RFA-US catheters (29) and the development of light delivery mechanisms utilized for intracardiac laser ablation (30).

Additionally, due to the temperature dependence of $\beta(T)$ (Equation 1), thermographic PA (tPA) mapping with high thermal and temporal resolutions (< 1 K and ~ 1 s, respectively) is possible (18,21,31). Guidance of myocardial ablation procedures represents an ideal application of tPA mapping as PA imaging has the potential to provide thermographic information co-registered with anatomical (US) and molecular (sPA) information. This feature of PA imaging has potential for both RF and cryoablation guidance. Future work will focus on providing concurrent US, sPA and tPA imaging data during an ablation procedure.

Conclusion

In conclusion, for this initial study, we demonstrate the feasibility of using sPA imaging to provide 3-D visualizations of ablated and non-ablated myocardium in an excised porcine myocardial ablation model. When compared with co-registered stained gross pathology, sPA imaging achieved sub-millimeter accuracy in identifying lesion position and extent and reliably characterized tissue to depths of 3 mm, including identifying adjacent and non-contiguous lesions. These initial results suggest that sPA imaging, with its molecular specificity and high spatial resolution, may be well suited as a clinical tool to guide trans-catheter ablation of atrial arrhythmia.

Supplementary Material

Refer to Web version on PubMed Central for supplementary material.

Acknowledgments

None

Funding Sources:

NIH Grant: NIH-EB007507 - Comprehensive Training Program in Imaging Science and Informatics.

Glossary

AF	atrial fibrillation
RT	real-time
RF	radio-frequency
OCT	optical coherence tomography
ARFI	acoustic radiation force impulse
US	ultrasound
PA	photoacoustic
Hb	deoxy-hemoglobin
sPA	spectroscopic photoacoustic
3-D	Three-dimensional
CBR	contrast-to-background ratio
NTB	nitro-tetrazolium blue
TCM	tissue characterization map
FOV	field of view
tPA	thermographic photoacoustic

References

1. Roger VL, Go AS, Lloyd-Jones DM, et al. Heart disease and stroke statistics--2012 update: a report from the American Heart Association. Circulation. 2012; 125:e2–e220. [PubMed: 22179539]
2. Miyasaka Y, Barnes ME, Gersh BJ, et al. Secular Trends in Incidence of Atrial Fibrillation in Olmsted County, Minnesota, 1980 to 2000, and Implications on the Projections for Future Prevalence. Circulation. 2006; 114:119–125. [PubMed: 16818816]
3. Wolf PA, Abbott RD, Kannel WB. Atrial fibrillation as an independent risk factor for stroke: the Framingham Study. Stroke. 1991; 22:983–988. [PubMed: 1866765]
4. Wolf PA, Mitchell JB, Baker CS, Kannel WB, D'Agostino RB. Impact of atrial fibrillation on mortality, stroke, and medical costs. Archives of Internal Medicine. 1998; 158:229–234. [PubMed: 9472202]
5. Benjamin EJ, Wolf PA, D'Agostino RB, Silbershatz H, Kannel WB, Levy D. Impact of atrial fibrillation on the risk of death: the Framingham Heart Study. Stroke. 1998; 98:946–952.

6. Shah D. A critical appraisal of cardiac ablation technology for catheter-based treatment of atrial fibrillation. Expert Review of Medical Devices. 2010; 8:49–55. [PubMed: 21158540]
7. Cappato R, Calkins H, Chen S-A, et al. Updated Worldwide Survey on the Methods, Efficacy, and Safety of Catheter Ablation for Human Atrial Fibrillation. Circulation: Arrhythmia and Electrophysiology. 2010; 3:32–38. [PubMed: 19995881]
8. Santangeli P, Di Biase L, Pelargonio G, Burkhardt JD, Natale A. The pharmaceutical pipeline for atrial fibrillation. Annals of Medicine. 2011; 43:13–32. [PubMed: 21166558]
9. Haïssaguerre M, Jaïs P, Shah DC, et al. Spontaneous initiation of atrial fibrillation by ectopic beats originating in the pulmonary veins. The New England Journal of Medicine. 1998; 339:659–666. [PubMed: 9725923]
10. Di Biase L, Santangeli P, Natale A. How to ablate long-standing persistent atrial fibrillation? Curr Opin Cardiol. 2013; 28:26–35. [PubMed: 23207492]
11. Rosenbaum R, Greenspon AJ, Smith M, Walinsky P. Advanced radiofrequency catheter ablation in canine myocardium. American Heart Journal. 1994; 127:851–857. [PubMed: 8154424]
12. Petersen HH, Chen X, Pietersen A, Svendsen JH, Haunsø S. Lesion Dimensions During Temperature-Controlled Radiofrequency Catheter Ablation of Left Ventricular Porcine Myocardium : Impact of Ablation Site, Electrode Size, and Convective Cooling. Circulation. 1999; 99:319–325. [PubMed: 9892601]
13. Ranjan R, Kholmovski EG, Blauer J, et al. Identification and Acute Targeting of Gaps in Atrial Ablation Lesion Sets Using a Real-Time Magnetic Resonance Imaging System. Circulation: Arrhythmia and Electrophysiology. 2012; 5:1130–1135. [PubMed: 23071143]
14. Kolandaivelu A, Zviman MM, Castro V, Lardo AC, Berger RD, Halperin HR. Noninvasive Assessment of Tissue Heating During Cardiac Radiofrequency Ablation Using MRI Thermography / Clinical Perspective. Circulation: Arrhythmia and Electrophysiology. 2010; 3:521–529. [PubMed: 20657028]
15. Fleming CP, Quan KJ, Wang H, Amit G, Rollins AM. In vitro characterization of cardiac radiofrequency ablation lesions using optical coherence tomography. Opt. Express. 2010; 18:3079–3092. [PubMed: 20174138]
16. Eyerly SA, Hsu SJ, Agashe SH, Trahey GE, Li Y, Wolf PD. An in vitro assessment of acoustic radiation force impulse imaging for visualizing cardiac radiofrequency ablation lesions. Journal of Cardiovascular Electrophysiology. 2010; 21:557–563. [PubMed: 20021518]
17. Eyerly SA, Bahnson TD, Koontz JI, et al. Intracardiac Acoustic Radiation Force Impulse Imaging: A Novel Imaging Method for Intraprocedural Evaluation of Radiofrequency Ablation Lesions. Heart Rhythm. 2012; 9:1855–1862. [PubMed: 22772134]
18. Beard P. Biomedical photoacoustic imaging. Interface Focus. 2011; 1:602–631. [PubMed: 22866233]
19. Xu M, Wang L V. Photoacoustic imaging in biomedicine. Review of Scientific Instruments. 2006; 77:41101.
20. Bouchard R, Dana N, Di Biase L, Natale A, Emelianov S. Photoacoustic characterization of radiofrequency ablation lesions. Proceedings of SPIE Vol. 8223 International Society for Optics and Photonics. 2012:82233K–1–6.
21. Shah J, Park S, Aglyamov S, et al. Photoacoustic imaging and temperature measurement for photothermal cancer therapy. Journal of Biomedical Optics. 2008; 13:034024–034029. [PubMed: 18601569]
22. Wang B, Karpiouk A, Yeager D, et al. Intravascular photoacoustic imaging of lipid in atherosclerotic plaques in the presence of luminal blood. Optics Letters. 2012; 37:1244–1246. [PubMed: 22466209]
23. Ntziachristos V: Going deeper than microscopy: the optical imaging frontier in biology. Nature Methods. 2010; 7:603–614. [PubMed: 20676081]
24. Swartling J, Pålsson S, Platonov P, Olsson SB, Andersson-Engels S, Palsson S. Changes in tissue optical properties due to radio-frequency ablation of myocardium. Medical & Biological Engineering & Computing. 2003; 41:403–409. [PubMed: 12892362]

25. Thomsen SL, Jacques SL, Flock ST. Microscopic correlates of macroscopic optical property changes during thermal coagulation of myocardium. Proceedings of the Society of Photo-Optical Instrumentation Engineers Vol. 1202 International Society for Optics and Photonics. 1990:2–11.

26. Mallidi S, Luke GP. Emelianov S: Photoacoustic imaging in cancer detection, diagnosis, and treatment guidance. Trends in Biotechnology. 2011; 29:213–221. [PubMed: 21324541]

27. Ramkissoon RA. Macroscopic identification of early myocardial infarction by dehydrogenase alterations. Journal of Clinical Pathology. 1966; 19:479–481. [PubMed: 5919360]

28. Prahl, S. Molar Extinction Coefficients of Hemoglobin and oxy-Hemoglobin. School of Medicine, Oregon Health and Science University; Portland, OR, USA: http://omlc.ogi.edu/spectra/hemoglobin/index.html

29. Wright M, Harks E, Deladi S, et al. Real-time lesion assessment using a novel combined ultrasound and radiofrequency ablation catheter. Heart Rhythm. 2011; 8:304–312. [PubMed: 21044698]

30. Dukkipati SR, Neuzil P, Kautzner J, et al. The durability of pulmonary vein isolation using the visually guided laser balloon catheter: Multicenter results of pulmonary vein remapping studies. Heart Rhythm. 2012; 9:919–925. [PubMed: 22293143]

31. Pramanik M, Wang LV. Thermoacoustic and photoacoustic sensing of temperature. Journal of Biomedical Optics. 2009; 14:54024–54027.

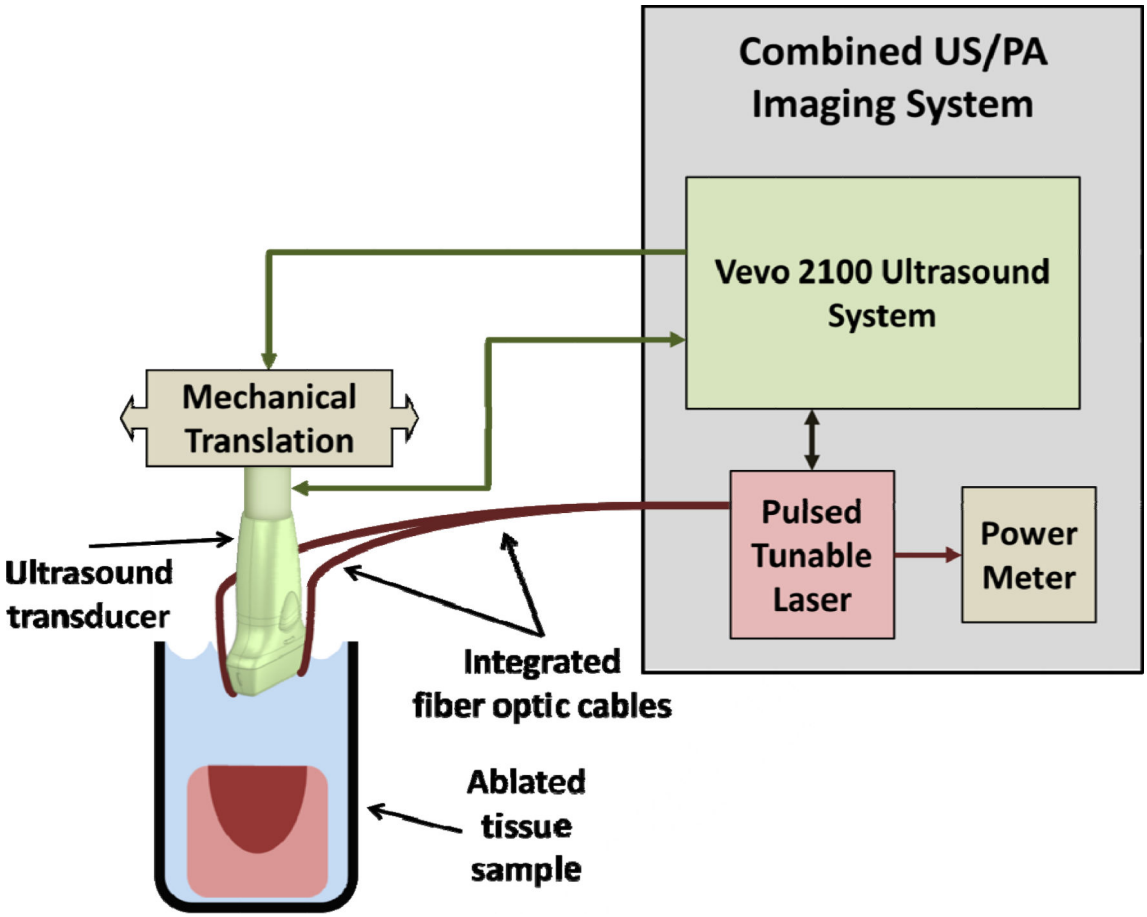

Figure 1.
Schematic of combined PA/US imaging system.

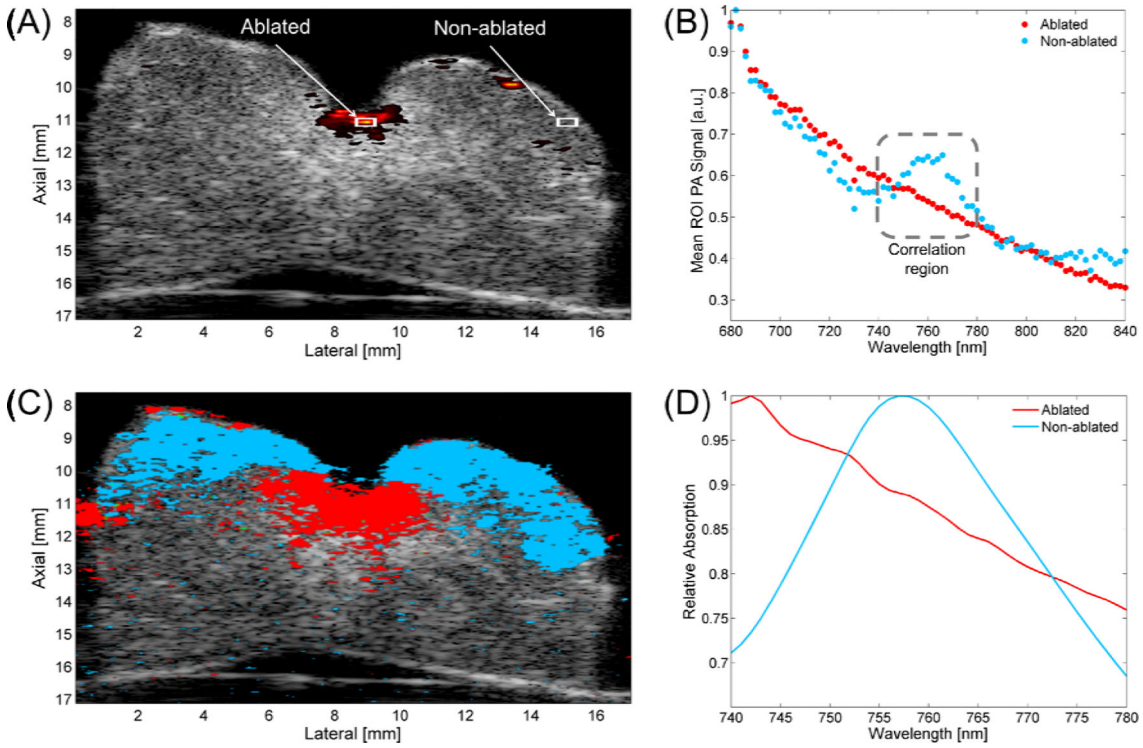

Figure 2.

Single-wavelength PA image (710 nm) overlaying US image with Ablated and Non-ablated ROIs (A). Mean ROI photoacoustic signal plotted vs. wavelength (B). Tissue characterization map (TCM) (C). Reference spectra for Ablated (averaged over eight samples from two hearts) and Non-ablated (derived from optical extinction data from deoxy-Hb) tissue (D).

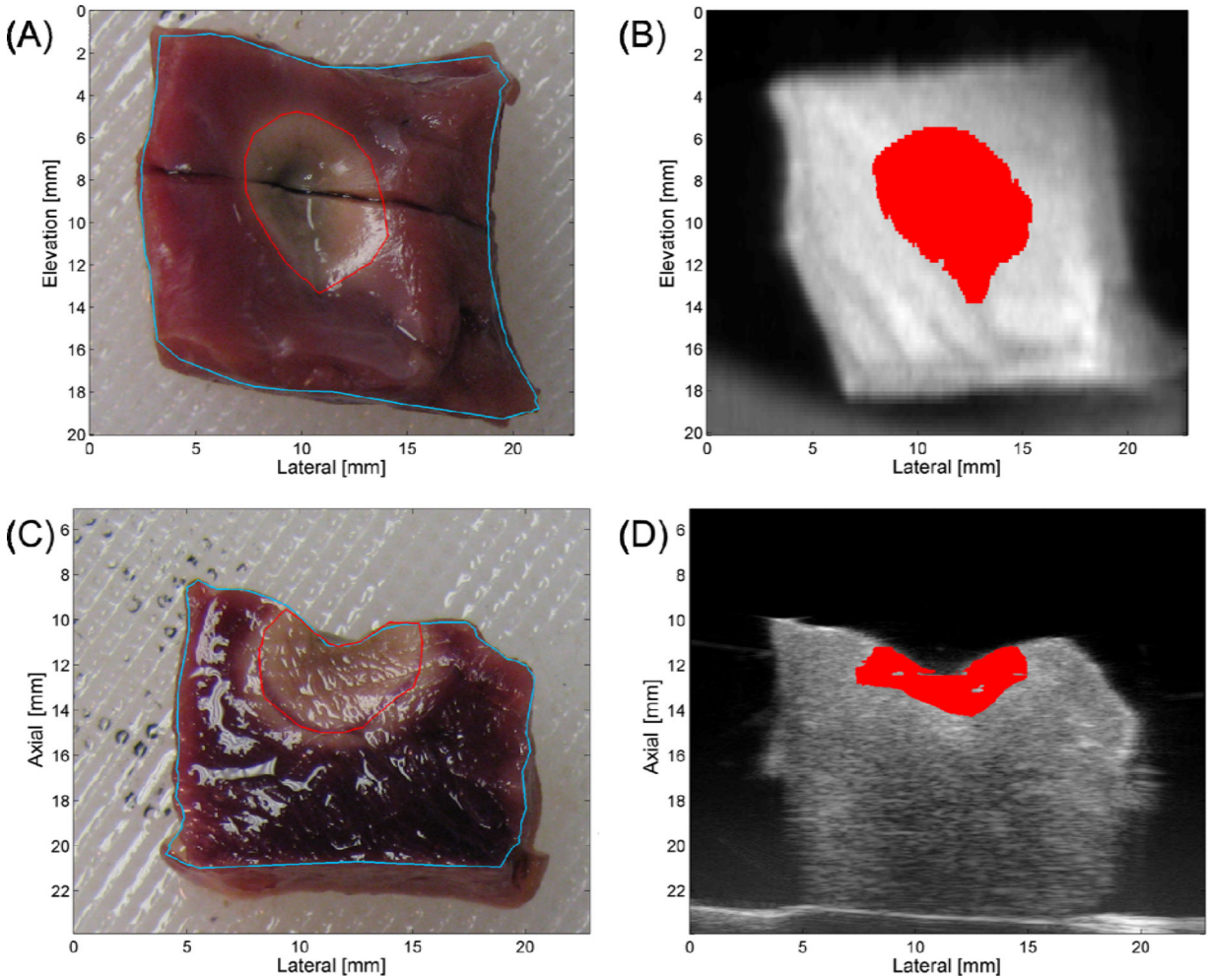

Figure 3.

Top-view (A) and side-view (C) stained sample gross pathology with sample-boundary (blue) and Ablated-region (red) segmentation. Matching top- (B) and side-view (D) TCM-US images with segmented ablated region (red).

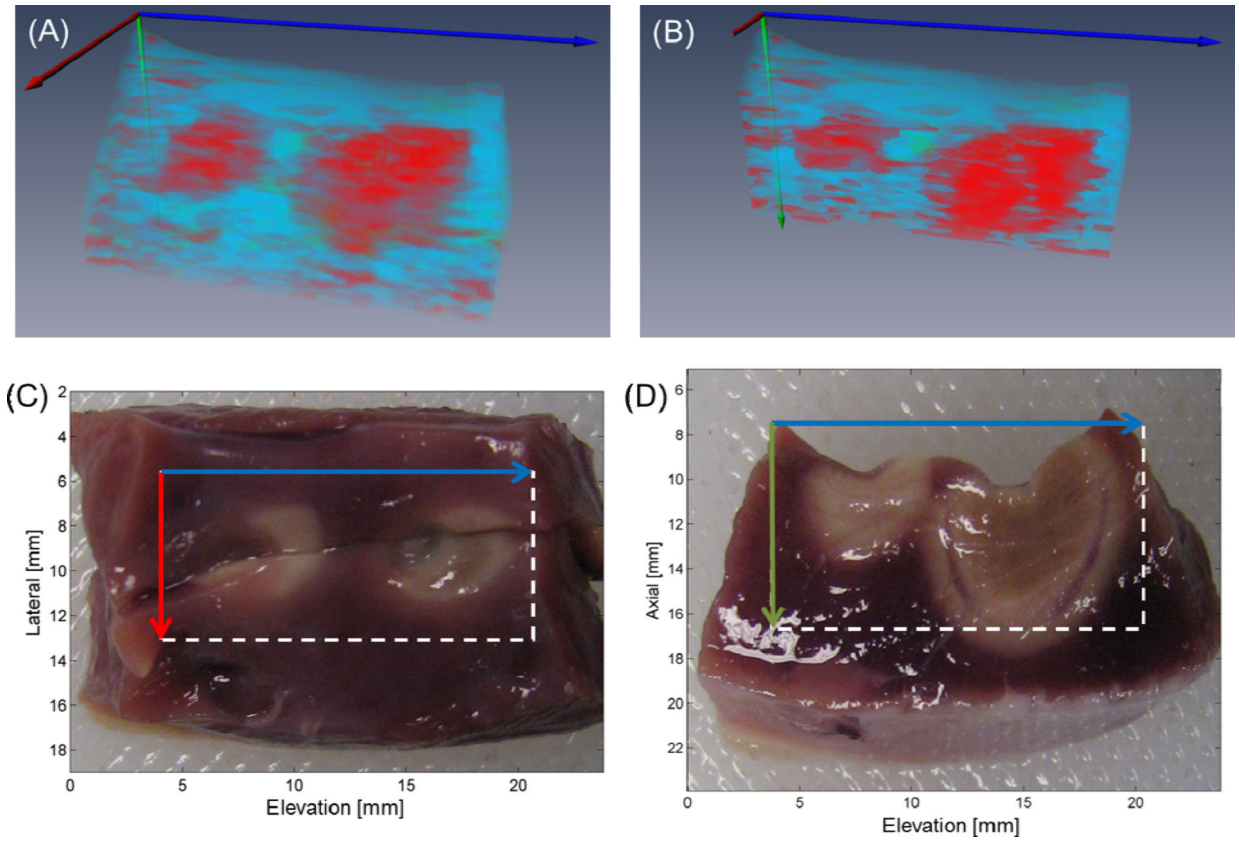

Figure 4.

Three-dimensional rendering (A) of TCM volume with clipping plane corresponding to tissue bisection (B). Matching top- (C) and side-view (D) gross pathology photographs with axes and FOVs indicated by arrows and boxes, respectively.

Table 1

Comparison of segmentation metrics from top- and side-view gross pathology and TCM/US registrations.

Lesion dimension statistics (*n* = 6 samples total)							
	Top-view orientation			Side-view orientation			
	Lateral (mm)	Elevation (mm)	Segmented Area (mm^2)	Axial (mm)	Lateral (mm)	Elevation (mm)	Segmented Area (mm^2)
TCM offset	0.4 ± 0.4	0.0 ± 0.7	-	1.2 ± 0.8	0.1 ± 0.7	0.9 ± 1.5	-
TCM extent	7.4 ± 1.8	7.3 ± 1.6	37.8 ± 15.8	3.4 ± 1.0	8.0 ± 1.4	6.3 ± 1.9	14.5 ± 4.9
Gross pathology extent	6.5 ± 1.9	8.3 ± 1.5	41.8 ± 16.4	5.3 ± 1.0	7.8 ± 1.4	10.9 ± 3.7	30.7 ± 10.1
Area agreement	-	-	69 ± 11%	-	-	-	36 ± 18%